Materials Transactions, Vol. 65, No. 9 (2024) pp. 1041 to 1048
Special Issue on Materials Science on High-Entropy Alloys II

Alloy Design and Solidification Microstructure of Ti-Zr-Hf-Ag-V Multi-Component Alloys with a Dual Bcc Structure

Takeshi Nagase[1,*], Mitsuharu Todai[2], Satoshi Ichikawa[3], Aira Matsugaki[4] and Takayoshi Nakano[4]

[1]*Department of Materials and Synchrotron Radiation Engineering, Graduate School of Engineering, University of Hyogo, Himeji 671-2280, Japan*
[2]*Department of Environmental Materials Engineering, National Institute of Technology, Niihama College, Niihama 792-8580, Japan*
[3]*Research Center for Ultra-High Voltage Electron Microscopy, Osaka University, Ibaraki 567-0047, Japan*
[4]*Division of Materials and Manufacturing Science, Graduate School of Engineering, Osaka University, Suita 565-0871, Japan*

$TiZrHfAgV_{0.2}$ ($Ti_{23.8}Zr_{23.8}Hf_{23.8}Ag_{23.8}V_{4.8}$, at%) high entropy alloys (HEAs) with a dual bcc structure were developed. Fine lamella structure was observed in the arc-melted ingots and melt-spun ribbons. The $TiZrHfAgV_{0.2}$ HEAs with a dual bcc phase structure were designed by exploiting the concept of immiscibility of the constituent elements. The immiscibility of the constituent elements in the multi-component alloys was discussed using the mixing enthalpy ($\Delta H_{i\text{-}j}$) matrix of the i-j elements, binary phase diagrams with liquid miscibility gap, and the thermodynamic calculations. [doi:10.2320/matertrans.MT-MA2024009]

(Received May 1, 2024; Accepted June 21, 2024; Published August 25, 2024)

Keywords: *high entropy alloys, metals and alloys, microstructure, solidification, liquid phase separation*

1. Introduction

New structural and functional metallic materials have gained immense attention owing to the increasing demands of sustainable development goals. Recently, high-entropy alloys (HEAs) have evolved as a new category of structural and functional materials [1–6]. Various definitions of HEAs have been suggested [5, 6]. In this, study, we used the entropy-based definition: $\Delta S_{mix} \geq 1.5R$, where ΔS_{mix} is the mixing entropy of the ideal and regular solutions in the alloys and R is the gas constant. Not only single phase HEAs but also dual-phase HEAs have also been attracting attention. The following three processes can be considered to be the typical routes for the formation of dual phase structure during the solidification of the thermal melt and the cooling in high entropy casting alloys without the subsequent thermal annealing: (1) Liquid phase separation (LPS) and the solidification of the separated liquid phases, (2) eutectic reaction of a thermal melt during the solidification, and (3) solid-state reaction. The formation of a dual phase structure composed with dendrite and inter-dendrite regions were not considered in the present study. The alloy design focusing on dual phase formation based on the immiscibility of the constituent elements in multi-component alloys are related with (1) and (3). The present study was reported the alloy design with the immiscibility of the constituent elements and liquid phase separation in multi-component alloys.

LPS has been reported in various HEA systems such as Al-Co-Cr-Cu-Ni-Ag [7], Al-Cr-Cu-Fe-Ni [8, 9], Co-Ni-Cu-Al-Cr [10], Co-Cr-Cu-Fe-Mo-Ni [11], Co-Cr-Cu-Fe-Ni [12–15], Cr-Cu-Fe-Mo-Ni [16], Co-Cu-Fe HEAs with Al, Cr, Mn, Ni, V or Ti [17], Co-Cr-Cu-Fe-Ni-Sn [18], Co-Cr-Fe-Mn-Ni-Ag [19], Co-Cr-Fe-Mn-Ni-Cu-B [19], Al-Cr-Fe-Ni-Mo [20], Co-Cr-Mo-Fe-Mn-W-Ag [21], and Ti-Zr-Hf-Y-La [22]. LPS is a general phenomenon in HEAs [23]. $TiZrHfYLa_{0.2}$ HEAs with a dual HCP structure [22] have been designed based on the concept of immiscibility of the constituent elements. Ti-Zr-Hf-Y-La alloy systems have been designed based on the LPS tendency of Ti-La [24–26] and Ti-Y [27] Ti-rare earth element systems.

HEAs were well known to be classified into several alloy groups [1–6], and the major two groups are (a) 3d-HEAs whose main constituent elements are 3-d transition metals and (b) Refractory High Entropy Alloys (RHEAs) and High Entropy Alloys for metallic biomaterials (BioHEAs) whose main constituent elements are 4th elements of Ti, Zr and Hf elements. Most of the reports on the liquid separation phenomenon in HEAs were related to 3d-HEAs as described above, and there are only few reports on liquid separation in RHEAs and BioHEAs. Motivated by the development of $TiZrHfYLa_{0.2}$ HEAs with a dual HCP structure [22], in this study, we designed $TiZrHfAgV_{0.2}$ HEAs by using the concepts of atomic pairing and liquid phase separation tendency in HEAs with Ti, Zr and Hf elements. The alloy design via the mixing enthalpy of i-j element pairs ($\Delta H_{i\text{-}j}$) and thermodynamic calculation, and the fabrication and solidification microstructure of $TiZrHfAgV_{0.2}$ HEAs with a dual BCC structure was reported.

2. Alloy Design

Combining the thermodynamic calculations and the value of $\Delta H_{i\text{-}j}$ among the constituent elements is an efficient approach for designing multi-component LPS-type amorphous alloys [28, 29] and LPS-type HEAs [19, 21, 22]. For the design of the new HEAs with 4th elements of Ti, Zr and Hf elements and the immiscibility of the constituent elements in multi-component alloys with the thermodynamic calculation and the value of $\Delta H_{i\text{-}j}$, we came up with HEAs with Ti-Ag and Zr-Ag pairs.

Figure 1 show the assessment map of the binary phase diagrams among Ti, Zr, Hf, Ag, and V elements in SGTE2022 thermodynamic database. In the present study, the thermodynamic calculation was performed by FactSage ver8.3 and SGTE2022 thermodynamic database with and without aiMP database. Binary Ti-Ag, Zr-Ag and V-Ag phase

*Corresponding author, E-mail: t-nagase@eng.u-hyogo.ac.jp

	Ti	Zr	Hf	Ag	V
Ti		○	○	○	○
Zr			○	○	○
Hf				×	○
Ag					○
V					

Fig. 1 The assessment map of the binary phase diagrams among Ti, Zr, Hf, Ag, and V elements in SGTE2022.

diagrams were assessed in SGTE2022. The thermal equilibrium phase diagrams of Ti-Ag [30] and Zr-Ag [31–35] show a flat liquidus. The existence of metastable liquid miscibility gaps has been confirmed in Ti-Ag [36] and Zr-Ag alloys [32] by experimental observations and thermodynamic calculations, respectively. V-Ag alloys exhibit immiscible liquid states [37]. Figure 2 shows the phase diagrams of Ti-Ag, Zr-Ag and V-Ag binary alloys with liquid miscibility gap constructed by the FactSage (ver8.3) and SGTE2022 database. The Ti-Ag, Zr-Ag and Ag-V binary phase diagrams were assessed in SGTE2022 database (Fig. 1), and the aiMP (ver. 8.3) database was not used in the thermodynamic calculation results shown in Fig. 2. In the Ti-Ag (Fig. 2(a)) and Zr-Ag (Fig. 2(b)) binary phase diagrams, metastable liquid miscibility gaps (denoted by dotted red lines) were observed below the flat liquidus line. Monotectic-type phase diagram of Ag-V, which was constructed by thermodynamic calculations, is shown in Fig. 2(c). Binary phase diagrams shown in Fig. 2 are corresponding to the previous reports [30–37], and indicate the repulsive interaction between Ti-Ag, Zr-Ag and V-Ag atomic pairs in the liquid state.

Figure 3 shows the mixing enthalpy matrix of $\Delta H_{i\text{-}j}$ among Ti, Zr, Hf, Ag and V elements. The values of $\Delta H_{i\text{-}j}$ were obtained from the literature [38]. Large positive $\Delta H_{i\text{-}j}$ values are favorable for LPS. The large positive value for the V-Ag pair (+17) was consistent with the liquid state miscibility [37] and monotectic-type phase diagram of Ag-V constructed by thermodynamic calculations (Fig. 2(c)). Ti-Ag and Zr-Ag showed negative $\Delta H_{i\text{-}j}$ values (−2 in Ti-Ag, −20 in Zr-Ag) (Fig. 3). This can be attributed to the existence of Ti-Ag and Zr-Ag intermetallic compounds [30–35] in the phase diagrams of Ti-Ag (Fig. 2(a)) and Zr-Ag (Fig. 2(b)) constructed by thermodynamic calculations. In the Ti-Ag (Fig. 2(a)) and Zr-Ag (Fig. 2(b)) phase diagrams, metastable liquid miscibility gaps (denoted by dotted red lines) were observed below the flat liquidus line. In spite of their negative $\Delta H_{i\text{-}j}$ values (Fig. 3), the Ti-Ag and Zr-Ag alloy systems showed LPS tendency, as clarified by their phase diagrams (Figs. 2(a) and 2(b)). The immiscibility characteristics of Ti-Ag alloys (metastable liquid miscibility gap as determined from thermodynamic calculations and negative $\Delta H_{i\text{-}j}$ values) are different from those of Ti-rare earth alloys with LPS such as Ti-La, Ti-Er, Ti-Ce, Ti-Nd, and Ti-Y (liquid state miscibility in phase diagrams and positive $\Delta H_{i\text{-}j}$ values) [28, 29, 39–41]. These factors make the designing of HEAs with Ti-Ag and Zr-Ag atomic pairs difficult.

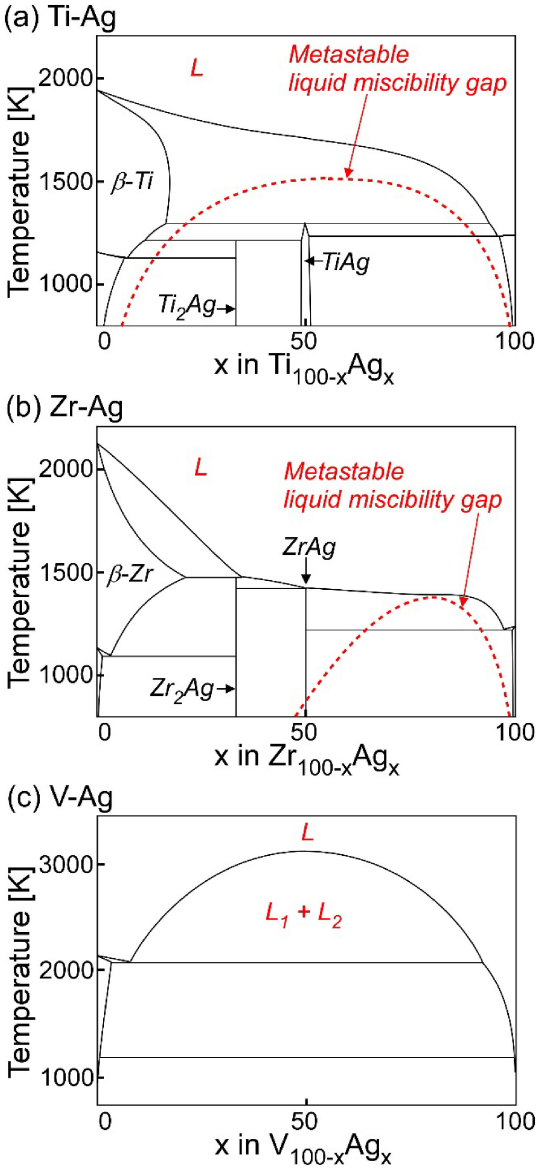

Fig. 2 Ti-Ag, Zr-Ag and V-Ag binary phase diagrams with liquid miscibility gap constructed by thermodynamic calculation using FactSage ver8.3 and SGTE2022. (a) Ti-Ag phase diagram with metastable liquid miscibility gap, (b) Zr-Ag phase diagram with metastable liquid miscibility gap, (c) V-Ag phase diagram with monotectic reaction.

	Ti	Zr	Hf	Ag	V
Ti		0	0	-2	-2
Zr			0	-20	-4
Hf				-13	-2
Ag					17
V					

Fig. 3 Mixing enthalpy matrix of i-j pairs ($\Delta H_{i\text{-}j}$) in Ti-Zr-Hf-Ag-V alloy system.

Based on the above-described alloy systems, Ti-Zr-Hf-Ag-V five component HEA was designed as the first step of the alloy design by combining Ti-Ag, Zr-Ag, and V-Ag immiscible alloy systems according to their phase dia-

grams. As the next step, $TiZrHfAlV_x$ alloy was considered as the non-equiatomic high entropy alloy because of the difficulty in the fabrication of the arc-melted ingots with the residual V lumps in the equiatomic TiZrHfAgV alloy. For satisfying the $\Delta S_{mix} \geq 1.5R$ in the nominal alloy composition, $TiZrHfAgV_{0.2}$ alloy was designed. The alloy parameters of ΔS_{mix}, heat of mixing (ΔH_{mix}), δ and Ω parameters for predicting the solid solution formation [5, 6] in $TiZrHfAgV_{0.2}$ were the followings: $\Delta S_{mix} = 1.51R$, $\Delta H_{mix} = -7.5\,kJ\,mol^{-1}$, $\delta = 5.9$, $\Omega = 3.3$. The alloy parameters imply the high solid solution formation tendency in $TiZrHfAgV_{0.2}$ alloy.

In order to discuss the immiscibility of the constituent elements in multi-component $TiZrHfAgV_{0.2}$ alloy in more detail, the thermodynamic calculation using aiMP database was performed. aiMP and aiOQ are developed based on *ab-initio* data from Materials Project [42, 43] and Open Quantum Materials Database [44, 45] as well as own data and developed machine learning models as input by GTT-Technologies [46]. Figure 4 shows the equilibrium calculation results of $TiZrHfAgV_{0.2}$ alloy. Hf-Ag phase diagram is not assessed in SGTE2022 database (Fig. 1). Figure 4(a) shows the equilibrium calculation results of $TiZrHfAgV_{0.2}$ alloy constructed by SGTE2022 database without aiMP database. The BCC single phase (indicated by the index BCC-1 and blue highlight) as the thermal equilibrium state was observed at temperatures lower than solidus temperature (Fig. 4(a)). The single BCC phase was not stable at the low temperature region and HCP phase appeared as a thermal

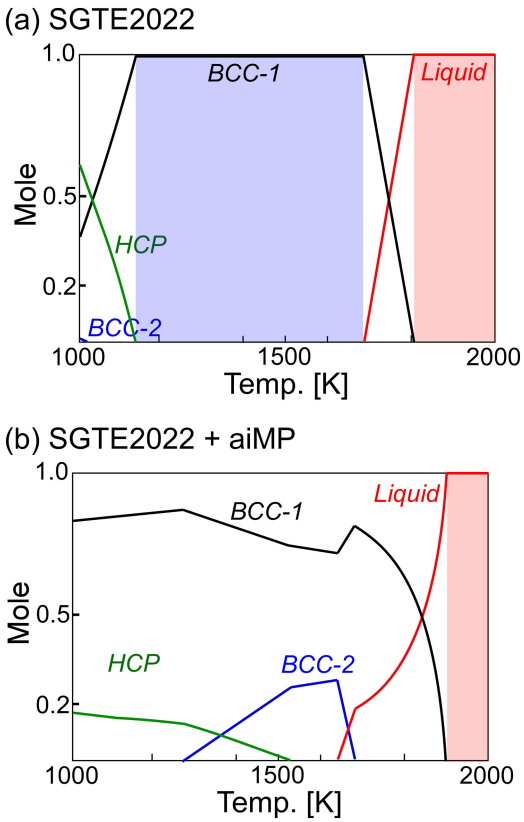

Fig. 4 Equilibrium calculation results of $TiZrHfAgV_{0.2}$ alloy. (a) SGTE2022 database without the thermodynamic assessment for binary Hf-Ag phase diagram. aiMP database was not used. (b) SGTE2022 + aiMP database.

Table 1 Rough estimation of the chemical composition of BCC phases in TiZrHfAgV0.2 alloy estimated by the thermodynamic calculation using FactSage ver 8.3 and SGTE2022 + aiMP database (at%).

Phases	Ti	Zr	Hf	Ag	V
BCC-1	23.2	25.3	22.6	28.2	0.0
BCC-2	25.5	19.7	27.1	11.9	15.9

equilibrium phase (Fig. 4(a)). Figure 4(b) shows the equilibrium calculation results of $TiZrHfAgV_{0.2}$ alloy constructed by SGTE2022 and aiMP database. It should be denoted that Fig. 4(b) is available only for the reference data because the accuracy of thermodynamic data in the aiMP database has not yet been performed in detail. Dual BCC phases indicated by the index BCC-1 and BCC-2 were appeared at the temperature below solidus temperature in Fig. 4(b).

Table 1 shows the chemical composition of BCC-1 and BCC-2 at 1600 K in the $TiZrHfAgV_{0.2}$ alloy predicted by SGTE2022 and aiMP database, where the data shown in Table 1 must be used only for the reference data. In Table 1, BCC-1 contains Ti, Zr, Hf and Ag elements near the equiatomic composition without V element, while BCC-2 contains Ti, Zr, Hf, Ag and V elements. The thermodynamic calculation results used SGTE2022 and aiMP database implies the formation of mutt-component dual BCC phases consisted with V-containing Ti-Zr-Hf-Ag-V and Ag-rich Ti-Zr-Hf-Ag BCC phases. The absence of the Hf-Ag atom pair in the thermodynamic calculation has a significant effect on the calculations of multi-component Ti-Zr-Hf-Ag-V alloys. It is difficult to discuss the cause of the difference between the thermodynamic calculation results in Fig. 4(a) and Fig. 4(b), because the aiMP database contains machine learning models.

3. Experimental Procedures

Arc-melted ingots of $TiZrHfAgV_{0.2}$ alloys were prepared by mixing the lumps of pure elements. The purity of the Ti, Zr, Ag, and V sources was above 3N (99.9%), while that of the Hf lumps was above 2N. Rapidly-solidified melt-spun ribbons were obtained using the single-roller melt-spinning method from a part of the arc-melted ingots. The cooling rate in the melt-spinning process is reported to be the order of 10^5 K/s [47, 48]. The cooling rate during melt-spinning process was two order higher than arc-melting process (approximately 2000 Ks^{-1}) [36, 49], was three order higher than centrifugal metallic mold casting (approximately 100 ~ 600 Ks^{-1}) [50]. The microstructures and constituent phases of the ingots were investigated using X-ray diffraction (XRD), scanning electron microscopy (SEM), and electron probe microanalysis (EPMA) with field-emission (FE) electron gun (FE-EPMA) and wave dispersive spectroscopy (WDS), transmission electron microscopy (TEM), and scanning transmission electron microscopy (STEM). The TEM and STEM specimens were prepared at room temperature by the ion-milling technique using Ar ions. The microstructure of arc-melted ingots and rapidly-solidified melt-spun ribbons was investigated in the present study focusing on the occurrence of liquid phase separation, single BCC phase

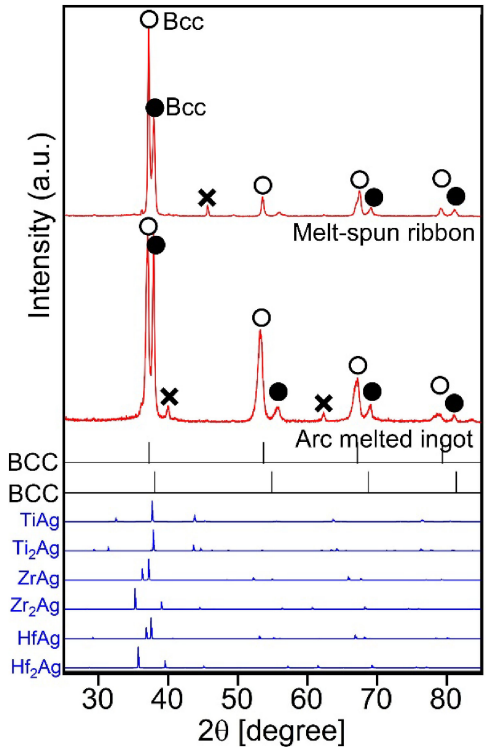

Fig. 5 XRD patterns of arc-melted ingots and the rapidly-solidified melt-spun ribbons of the $TiZrHfAgV_{0.2}$ alloy, together with the calculated XRD intensity profiles of BCC phases with difference lattice constants and intermetallic compounds.

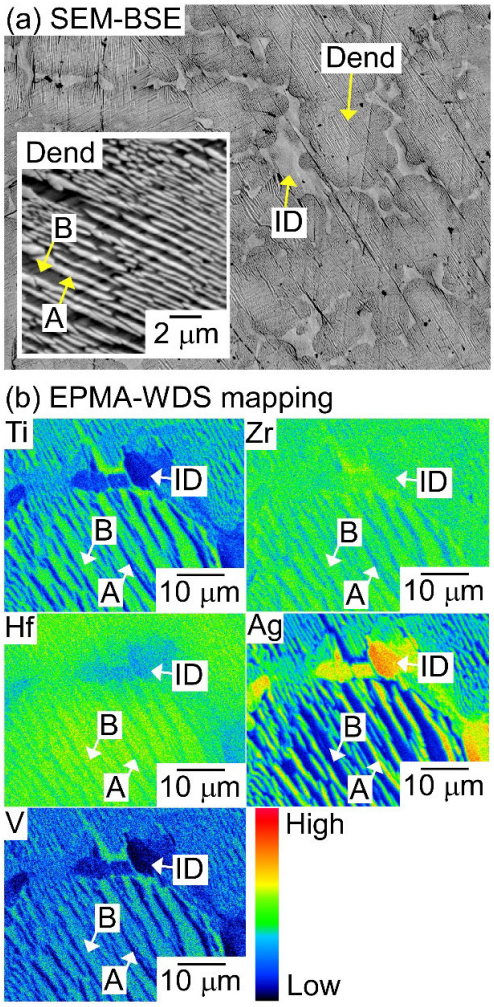

Fig. 6 Solidification microstructure of the arc-melted ingots in the $TiZrHfAgV_{0.2}$ alloy. (a) SEM-BSE images, the indexes Dend and ID denote the dendrite and inter-dendrite regions, respectively. The inset is the magnified image of the dendrite region. (b) EPMA-WDS mapping.

and/or dual BCC phase formation. FE-EPMA observation was performed via net-work tele-microscopy among University of Hyogo (Himeji, Hyogo, Japan), Osaka University (Ibaraki, Osaka, Japan) and National Institute of Technology, Niihama College (Niihama, Ehime, Japan).

4. Results

Figure 5 shows the XRD patterns of arc-melted ingots and rapidly-solidified melt-spun ribbons in the $TiZrHfAgV_{0.2}$ alloy, together with the peak positions of BCC phases with different lattice constants and the calculated XRD patterns of TiZr, Ti_2Ag, ZrAg, Zr_2Ag, HfAg, Hf_2Ag. The calculated XRD patterns were obtained using VESTA [51]. The majority of the sharp peaks in arc-melted ingots corresponded to the BCC phases indicated by the black solid (●) and black open (○) circles. Minor peak indicated by the black X mark (×) was not identified because of the low intensity peak and the few numbers in XRD patterns. Sharp peaks in melt-spun ribbons were also considered to be corresponding to dual BCC phases indicated by the indexes ● and ○.

Figure 6 shows the solidification microstructure of the arc-melted ingots in the $TiZrHfAgV_{0.2}$ alloy. SEM-Back Scattering Electron (BSE) images showed the typical solidification microstructure composed with dendrite region indicated by the indexes Dend and the inter-dendrite region indicated by the index ID (Fig. 6(a)). The typical solidification microstructures formed through liquid phase separation, such as macroscopically phase separated structure and/or emulsion like structure, were not observed in the arc-melted ingots. In Fig. 6(a), the inset is the magnified image focusing on the dendrite region indicated by the index Dend. The formation of the fine lamella structure composed with the white contrast region indicated by the index A and the gray contrast region indicated by the index B was observed in the dendrite region. EPMA-WDS elemental mapping results show the formation of Ag-rich (A) and V-rich (B) regions. Table 2 shows the WDS analysis results of the regions A and B in the dendrite region, together with the inter-dendrite region in Fig. 6. Compared with the multi-component Ti-Zr-Hf-Ag-V region (A) and Ti-Zr-Hf-Ag region (B), the Ag ratio in the region B is larger than that of the region A, while the V concentration in the region B is much lower than that of the region A. The formation of dual BCC phases with V-poor

Table 2 EPMA-WDS analysis results of arc-melted ingots in $TiZrHfAgV_{0.2}$ alloy (at%). The regions indicated by the index A and B are corresponding to these in SEM-BSE images shown in Fig. 6(a).

Position	Ti	Zr	Hf	Ag	V
Dend, A	22.3	21.3	24.9	28.0	3.5
Dend, B	35.8	23.0	28.2	6.6	6.4
ID	9.1	23.6	18.7	48.4	0.2

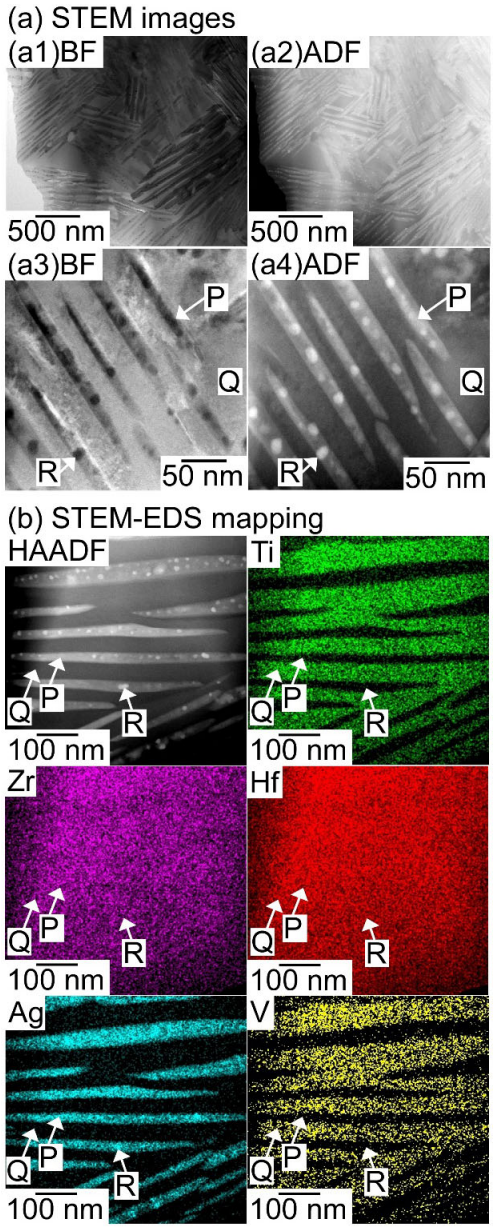

Fig. 7 Solidification microstructure of the rapidly-solidified melt-spun ribbons in the $TiZrHfAgV_{0.2}$ alloy. (a) STEM-BF and ADF images, (a3) and (a4) are the magnified image of (a1) and (a2), respectively. (b) STEM-EDS mapping.

region and Ag-rich regions in the arc-melted ingots were roughly corresponding to the thermodynamic calculation results with SGTE2022 and aiMP database shown in Fig. 4(b) and Table 1.

Figure 7 shows the solidification microstructure of the rapidly-solidified melt-spun ribbons in the $TiZrHfAgV_{0.2}$ alloy. The STEM-BF (Figs. 7(a1) and 7(a3)) and STEM annular dark field (ADF) (Figs. 7(a2) and 7(a4)) images shows the formation of the fine lamella structure. On the other hand, the typical solidification microstructure with liquid phase separation, namely, emulsion like structure reported in Ti-rare-earth-based alloys [24, 25] and Ti-Ag-based alloys [30, 52, 53], was not observed in melt-spun ribbons of a $TiZrHfAgV_{0.2}$ alloy. In the magnified STEM-ADF image (Fig. 7(a4)), the white contrast elongated phase (indicated by the index P) with spherical white contrast

Table 3 STEM-EDS analysis results of melt-spun ribbons in $TiZrHfAgV_{0.2}$ alloy (at%). The regions indicated by the indexes P, Q and R are corresponding to these in Fig. 7.

Position	Ti	Zr	Hf	Ag	V
P	4.5	19.1	19.3	56.6	0.5
Q	30.4	26.9	23.5	11.8	7.4
R	4.8	15.0	13.0	66.8	0.4

globules (indicated by the index R) was embedded in the gray-contrast matrix phase (indicated by the index Q). Figure 7(b) shows the STEM-EDS elemental mapping results of the alloys. The white contrast elongated phase observed in the STEM-ADF image (P) was rich in Zr, Hf, and Ag, while Ti, Zr, Hf, and V were predominant in the gray contrast matrix (Q). The white contrast globules in the STEM-ADF image (R) corresponded to the Ag-rich phase. The occurrence of the liquid phase separation phenomenon was not observed experimentally in the $TiZrHfAgV_{0.2}$ alloy.

5. Discussion

The formation of a dual BCC phase structure with a fine lamellar structure consisting of an Ag-rich phase and an Ag-poor phase was confirmed in both the arc-melted ingot (Figs. 5, 6, and Table 2) and the rapidly solidified ribbon (Figs. 5, 7 and Table 3). The formation of Ag-rich phase and Ag-poor phase is due to the immiscibility of Ti-Ag, Zr-Ag, V-Ag pairs in the phase diagrams shown in Fig. 2, a V-Ag pair shown in $\Delta H_{i\text{-}j}$ of Fig. 3, and the equilibrium calculation result with aiMP database shown in Fig. 4(b) and Table 1.

One may consider the possibility of the formation of TiAg-, ZrAg- and/or HfAg-based intermetallic compounds in inter-dendrite (ID) region in arc-melted ingots (Fig. 6 and Table 2) and the region P of the melt-spun ribbons (Fig. 7 and Table 3) from a view point of the chemical composition analysis results, ignoring the low accuracy of the STEM-EDS analysis in the multicomponent alloys. XRD pattern of the melt-spun ribbons shown in Fig. 3 was hardly explained by the formation of TiAg, ZrAg and HfAg. Zhou *et al.* examined the isothermal cross-section of an Ag-Ti-Zr ternary alloy system at 1023 K [54]. They found that no ternary compound was formed, Ti_2Ag and Zr_2Ag were nearly linear and formed Ag $(Ti, Zr)_2$ with the $C11_b$ structure, and the highest solubility of Ti in AgZr was about 20.9%, while that of Zr in AgTi was about 7.2%. The information of Ag-rich intermetallic compounds whose Ag concentration above 50 at% was not shown in the Ag-Ti-Zr ternary alloy phase diagram. Further discussion of the possibility of the formation of intermetallic compounds in the inter-dendrite (ID) region in the arc-melted ingots, and the region P in melt-spun ribbons was not achieved in this study because of the lack of the thermodynamically-assessed data related with Hf and the difficulty in carrying out the electron microscopy observations of multi-component alloys with a fine lamella structure.

It should be noted that there was no discrepancy between the experimentally observed formation tendency of the Ag-

poor and Ag-rich BCC phases in the arc-melted ingots and in melt-spun ribbons of the $TiZrHfAgV_{0.2}$ HEA and the alloy design via the binary phase diagrams with metastable liquid miscibility gap (Fig. 2), $\Delta H_{i\text{-}j}$, and the thermodynamic calculation with aiMP database. The alloy design based on the immiscibility of the constituent elements was found to be an efficient approach to develop dual-phase HEAs. An increase in the immiscibility of the constituent elements in the $TiZrHfAgV_{0.2}$ HEA resulted in the formation the dual BCC phase structure. A dual HCP structure is formed during the liquid phase separation in the $TiZrHfYLa_{0.2}$ HEA [22]. The difference in the occurrence of the liquid phase separation phenomenon in $TiZrHfAgV_{0.2}$ and $TiZrHfYLa_{0.2}$ [22] HEAs can be attributed to the difference between the liquid phase separation tendencies of Ti-Ag and Zr-Ag with metastable liquid miscibility gap in the phase diagrams and negative $\Delta H_{i\text{-}j}$ (Figs. 3 and 4) and Ti-La [26] and Ti-Y [27] (with a monotectic reaction of the liquid phase and positive $\Delta H_{i\text{-}j}$). The alloy design in HEAs with the enhancement the immiscibility among constituent elements was reported to be effective for the achievement of the good ductility and high mechanical strength in Co-Cr-Cu-Fe-Ni HEAs with liquid phase separation [14] and Co-Cr-Cu-Mn-Ni HEAs [55, 56]. These reports indicate the importance of the alloy design in HEAs with the immiscibility among constituent elements. Ti-Ag alloys are used in dental materials because of their biocompatibility, corrosion resistance, excellent mechanical properties, and machinability [57, 58]. Recently, Ti-containing HEAs have been developed for applications in metallic biomaterials (BioHEAs) [49, 59–64]. The alloy design method used in this study for developing the $TiZrHfAgV_{0.2}$ HEA will be helpful for developing Ti-Ag-based BioHEAs with the immiscibility among constituent elements.

The fine lamella structure formation during the solidification of the thermal melt and the cooling of specimens was observed in the $TiZrHfAgV_{0.2}$ HEA. The emulsion like structure in Ti-rare-earth-based alloys [24, 25] and Ti-Ag-based alloys [30, 52, 53], was not observed in the arc-melted ingots and melt-spun ribbons in the $TiZrHfAgV_{0.2}$ HEA. The fine lamella structure formation in the arc-melted ingots and melt-spun ribbons in the $TiZrHfAgV_{0.2}$ HEA was hardly explained by the liquid phase separation. One may consider that fine lamella structure formation the $TiZrHfAgV_{0.2}$ HEA may be explained by the eutectic reaction based on the concept of the eutectic high entropy alloys (EHEAs) such as $AlCoCrFeNi_{2.1}$ EHEAs [65–67]. As shown in Fig. 6(a), the fine lamella formation was observed in the dendrite region in the arc-melted ingots of the $TiZrHfAgV_{0.2}$ HEA. This implies that the fine lamella structure formation was not due to the eutectic reaction but the solid-state reaction. It should be noted here that the eutectic reaction during the solidification cannot be explained by the thermodynamic calculation shown in Fig. 4. Further investigation must be necessary for clarifying the fine lamella structure formation in arc-melted ingots and melt-spun ribbons in the $TiZrHfAgV_{0.2}$ HEA, and this will be reported in the future works.

6. Conclusions

In conclusion, the $TiZrHfAgV_{0.2}$ ($Ti_{23.8}Zr_{23.8}Hf_{23.8}Ag_{23.8}$-$V_{4.8}$, at%) HEA with a dual bcc structure was developed. The arc-melted ingots and melt-spun ribbons showed a fine lamella structure. $TiZrHfAgV_{0.2}$ HEA was designed based on the concept of immiscibility of the constituent elements by using mixing enthalpy, binary phase diagrams with stable and meta-stable liquid miscibility gap, and the thermodynamic calculations. The alloy design strategy used in this study will be helpful for the development of Ti-Ag-based metallic biomaterials and BioHEAs.

Acknowledgements

Funding: This work was partially supported by JSPS KAKENHI (Grant Number 21H00146, and 22H01816), and by the light metal education foundation, Inc.

REFERENCES

[1] B. Cantor, I.T.H. Chang, P. Knight and A.J.B. Vincent: Microstructural development in equiatomic multicomponent alloys, Mater. Sci. Eng. A **375–377** (2004) 213–218.

[2] J.W. Yeh, S.K. Chen, S.J. Lin, J.Y. Gan, T.S. Chin, T.T. Shun, C.H. Tsau and S.Y. Chang: Nanostructured High-Entropy Alloys with Multiple Principal Elements: Novel Alloy Design Concepts and Outcomes, Adv. Eng. Mater. **6** (2004) 299–303.

[3] Y. Zhang, Y.J. Zhou, J.P. Lin, G.L. Chen and P.K. Liew: Solid-Solution Phase Formation Rules for Multi-component Alloys, Adv. Eng. Mater. **10** (2008) 534–538.

[4] H. Inui, K. Kishida and Z. Chen: Recent Progress in Our Understanding of Phase Stability, Atomic Structures and Mechanical and Functional Properties of High-Entropy Alloys, Mater. Trans. **63** (2022) 394–401.

[5] B.S. Murty, J.-W. Yeh and S. Ranganathan: *High-Entropy Alloys*, 1st ed., (Elsevier, Amsterdam, 2014) ISBN 9780128002513.

[6] M.C. Gao, J.-W. Yeh, P.K. Liaw and Y. Zhang: *High-Entropy Alloys, Fundamentals and Applications*, 1st ed., (Springer, Berlin, 2016) ISBN 9783319270135.

[7] U.S. Hsu, U.D. Hung, J.W. Yeh, S.K. Chen, Y.S. Huang and C.C. Yang: Alloying behavior of iron, gold and silver in AlCoCrCuNi-based equimolar high-entropy alloys, Mater. Sci. Eng. A **460–461** (2007) 403–408.

[8] S. Guo, C. Ng and C.T. Liu: Anomalous solidification microstructures in Co-free $Al_xCrCuFeNi_2$ high-entropy alloys, J. Alloy. Compd. **557** (2013) 77–81.

[9] A. Munitz, S. Samuha, E. Brosh, S. Salhov, N. Derimow and R. Abbaschian: Liquid phase separation phenomena in $Al_{2.2}CrCuFeNi_2$ HEA, Intermetallics **97** (2018) 77–84.

[10] A. Munitz, M.J. Kaufman, J.P. Chandler, H. Kalaantari and R. Abbaschian: Melt separation phenomena in CoNiCuAlCr high entropy alloy containing silver, Mater. Sci. Eng. A **560** (2013) 633–642.

[11] P.H. Wu, N. Liu, W. Yang, Z.X. Zhu, Y.P. Lu and X.J. Wang: Microstructure and solidification behavior of multicomponent $CoCrCu_xFeMoNi$ high-entropy alloys, Mater. Sci. Eng. A **642** (2015) 142–149.

[12] N. Liu, P.H. Wu, P.J. Zhou, Z. Peng, X.J. Wang and Y.P. Lu: Rapid solidification and liquid-phase separation of undercooled $CoCrCuFe_xNi$ high-entropy alloys, Intermetallics **72** (2016) 44–52.

[13] P.H. Wu, N. Liu, P.J. Zhou, Z. Peng, W.D. Du, X.J. Wang and Y. Pan: Microstructures and liquid phase separation in multicomponent CoCrCuFeNi high entropy alloys, Mater. Sci. Technol. **32** (2016) 576–580.

[14] W.L. Wang, L. Hu, S.B. Luo, L.J. Meng, D.L. Geng and B. Wei: Liquid phase separation and rapid dendritic growth of high-entropy CoCrCuFeNi alloy, Intermetallics **77** (2016) 41–45.

[15] T. Guo, J. Li, J. Wang, Y. Wang, H. Kou and S. Niu: Liquid-phase separation in undercooled CoCrCuFeNi high entropy alloy, Intermetallics **86** (2017) 110–115.

[16] Z. Peng, N. Liu, S.Y. Zhang, P.H. Wu and X.J. Wang: Liquid-phase

separation of immiscible $CrCu_xFeMo_yNi$ high-entropy alloys, Mater. Sci. Technol. **33** (2017) 1352–1359.
[17] A. Munitz, M.J. Kaufman and R. Abbaschian: Liquid phase separation in transition element high entropy alloys, Intermetallics **86** (2017) 59–72.
[18] S. Wang, Z. Chen, L.C. Feng, Y.Y. Liu, P. Zhang, Y.Z. Hea, Q.Q. Menga and J.Y. Zhanga: Nano-phase formation accompanying phase separation in undercooled CoCrCuFeNi-3 at.% Sn high entropy alloy, Mater. Charact. **144** (2018) 516–521.
[19] T. Nagase, M. Todai and T. Nakano: Liquid Phase Separation in Ag-Co-Cr-Fe-Mn-Ni, Co Cr-Cu-Fe-Mn-Ni and Co-Cr-Cu-Fe-Mn-Ni-B High Entropy Alloys for Biomedical Application, Crystals **10** (2020) 527.
[20] A. Munitz, I. Edry, E. Brosh, N. Derimow, B.E. MacDonald, E.J. Lavernia and R. Abbaschian: Liquid phase separation in AlCrFeNi-$Mo_{0.3}$ high-entropy alloy, Intermetallics **112** (2019) 106517.
[21] T. Nagase, M. Todai and T. Nakano: Development of Co–Cr–Mo–Fe–Mn–W and Co–Cr–Mo–Fe–Mn–W–Ag High-Entropy Alloys Based on Co–Cr–Mo Alloys, Mater. Trans. **61** (2020) 567–576.
[22] T. Nagase, M. Todai and T. Nakano: Development of Ti–Zr–Hf–Y–La high-entropy alloys with dual hexagonal-close-packed structure, Scr. Mater. **186** (2020) 242–246.
[23] N. Derimow and R. Abbaschian: Liquid Phase Separation in High-Entropy Alloys—A Review, Entropy **20** (2018) 890.
[24] S.H. Whang: Rapidly solidified titanium alloys for high-temperature applications, J. Mater. Sci. **21** (1986) 2224–2238.
[25] S.A. Court, J.W. Sears, M.H. Loretto and H.L. Fraser: The effect of liquid phase separation on the microstructure of rapidly solidified titanium-Rare earth alloys, Mater. Sci. Eng. **98** (1988) 243–249.
[26] *Binary Alloy Phase Diagrams*, II ed., ed. by T.B. Massalski, "La-Ti", 2, (ASM international, Materials Park, Ohio, 1990) pp. 1479–1481.
[27] *Binary Alloy Phase Diagrams*, II ed., ed. by T.B. Massalski, "Ti-Y", 2, (ASM international, Materials Park, Ohio, 1990) pp. 2138–2139.
[28] T. Nagase, M. Suzuki and T. Tanaka: Formation of amorphous phase with crystalline globules in Fe–Cu–Nb–B immiscible alloys, J. Alloy. Compd. **619** (2015) 267–274.
[29] T. Nagase, M. Takemura, M. Matsumuro, M. Matsumoto and Y. Fujii: Design and microstructure analysis of globules in Al-Co-La-Pb immiscible alloys with an amorphous phase, Mater. Des. **117** (2017) 338–345.
[30] J.L. Murray and K.J. Bhansali: The Ag−Ti (Silver-Titanium) system, Bull. Alloy Phase Diagr. **4** (1983) 178–183.
[31] A. Decreton, P. Benigni, J. Rogez, G. Mikaelian, M. Barrachin, M. Lomello-Tafin, C. Antion, A. Janghorban and E. Fischer: Contribution to the description of the absorber rod behavior in severe accident conditions: An experimental investigation of the Ag–Zr phase diagram, J. Nucl. Mater. **465** (2015) 849–856.
[32] D.H. Kang and I.-H. Jung: Critical thermodynamic evaluation and optimization of the Ag–Zr, Cu–Zr and Ag–Cu–Zr systems and its applications to amorphous Cu–Zr–Ag alloys, Intermetallics **18** (2010) 815–833.
[33] X.C. He, H. Wang, H.S. Liu and Z.P. Jin: Thermodynamic description of the Cu–Ag–Zr system, Calphad **30** (2006) 367–374.
[34] I. Karakaya and W.T. Thompson: The Ag-Zr (silver-zirconium) system, J. Phase Equilibria **13** (1992) 143–146.
[35] K. Zhang, H. Zhao and Y. Zhou: An investigation of the Ag-Zr phase diagram, J. Less Common Met. **138** (1988) 173–177.
[36] T. Nagase, M. Matsumoto and Y. Fujii: Microstructure of Ti-Ag immiscible alloys with liquid phase separation, J. Alloy. Compd. **738** (2018) 440–447.
[37] J.F. Smith: The Ag−V (Silver-Vanadium) system, J. Phase Equilibria **2** (1981) 343–344.
[38] A. Takeuchi and A. Inoue: Classification of Bulk Metallic Glasses by Atomic Size Difference, Heat of Mixing and Period of Constituent Elements and Its Application to Characterization of the Main Alloying Element, Mater. Trans. **46** (2005) 2817–2829.
[39] *Binary Alloy Phase Diagrams*, II ed., ed. by T.B. Massalski, "Ce-Ti", 1, (ASM international, Materials Park, Ohio, 1990) pp. 746–748.
[40] *Binary Alloy Phase Diagrams*, II ed., ed. by T.B. Massalski, "Er-Ti", 1, (ASM international, Materials Park, Ohio, 1990) pp. 1039–1044.
[41] *Binary Alloy Phase Diagrams*, II ed., ed. by T.B. Massalski, "Nd-Ti", 2, (ASM international, Materials Park, Ohio, 1990) pp. 1723–1729.
[42] S.P. Ong, S. Cholia, A. Jain, M. Brafman, D. Gunter, G. Ceder and K.A. Persson: The Materials Application Programming Interface (API): A simple, flexible and efficient API for materials data based on REpresentational State Transfer (REST) principles, Comput. Mater. Sci. **97** (2015) 209–215.
[43] S.P. Ong, W.D. Richards, A. Jain, G. Hautier, M. Kocher, S. Cholia, D. Gunter, V.L. Chevrier, K.A. Persson and G. Ceder: Python Materials Genomics (pymatgen): A robust, open-source python library for materials analysis, Comput. Mater. Sci. **68** (2013) 314–319.
[44] J.E. Saal, S. Kirklin, M. Aykol, B. Meredig and C. Wolverton: Materials Design and Discovery with High-Throughput Density Functional Theory: The Open Quantum Materials Database (OQMD), JOM **65** (2013) 1501–1509.
[45] S. Kirklin, J.E. Saal, B. Meredig, A. Thompson, J.W. Doak, M. Aykol, S. Ruhl and C. Wolverton: The Open Quantum Materials Database (OQMD): assessing the accuracy of DFT formation energies, NPJ Comput. Mater. **1** (2015) 15010.
[46] https://gtt-technologies.de/, (assessed, 2024.04.18).
[47] R.W. Cahn: *Physical Metallurgy*, 3rd ed., (Elsevier Science Publishers, 1996) ISBN 9780444898753.
[48] H. Miyake, A. Furusawa, T. Ariyasu and A. Okada: Optical Measurement of Cooling Rate During Splat Cooling Process, J. Jpn. Foundrymen's Soc. **66** (1994) 734–738.
[49] T. Nagase, K. Mizuuchi and T. Nakano: Solidification Microstructures of the Ingots Obtained by Arc Melting and Cold Crucible Levitation Melting in TiNbTaZr Medium-Entropy Alloy and TiNbTaZrX (X = V, Mo, W) High-Entropy Alloys, Entropy **21** (2019) 483.
[50] T. Nagase, M. Takemura, M. Matsumuro and T. Maruyama: Solidification Microstructure of $AlCoCrFeNi_{2.1}$ Eutectic High Entropy Alloy Ingots, Mater. Trans. **59** (2018) 255–264.
[51] K. Momma and F. Izumi: *VESTA 3* for three-dimensional visualization of crystal, volumetric and morphology data, J. Appl. Cryst. **44** (2011) 1272–1276.
[52] T. Nagase, M. Matsumoto and Y. Fujii: PM-09 Microstructure of Ti-Nb-Ag Immiscible Alloys with Liquid Phase Separation, Microscopy **66** (2017) i22.
[53] T. Nagase: Alloy Design, Thermodynamics, and Electron Microscopy of Ternary Ti-Ag-Nb Alloy with Liquid Phase Separation, Materials **13** (2020) 5268.
[54] G. Zhou, H. Liu, L. Liu and Z. Jin: Determination of isothermal section of Ag-Ti-Zr ternary system at 1 023 K, J. Cent South Univ. Technol. **14** (2007) 750–752.
[55] G. Qin, R. Chen, P.K. Liaw, Y. Gao, X. Li, H. Zheng, L. Wang, Y. Su, J. Guo and H. Fu: A novel face-centered-cubic high-entropy alloy strengthened by nanoscale precipitates, Scr. Mater. **172** (2019) 51–55.
[56] G. Qin, R. Chen, P.K. Liaw, Y. Gao, L. Wang, Y. Su, H. Ding, J. Guo and X. Li: An as-cast high-entropy alloy with remarkable mechanical properties strengthened by nanometer precipitates, Nanoscale **12** (2020) 3965–3976.
[57] M. Takahashi, M. Kikuchi, Y. Takada and O. Okuno: Mechanical Properties and Microstructures of Dental Cast Ti-Ag and Ti-Cu Alloys., Dent. Mater. J. **21** (2002) 270–280.
[58] B.B. Zhang, Y.F. Zheng and Y. Liu: Effect of Ag on the corrosion behavior of Ti–Ag alloys in artificial saliva solutions, Dent. Mater. **25** (2009) 672–677.
[59] M. Todai, T. Nagase, T. Hori, A. Matsugaki, A. Sekita and T. Nakano: Novel TiNbTaZrMo high-entropy alloys for metallic biomaterials, Scr. Mater. **129** (2017) 65–68.
[60] S.P. Wang and J. Xu: TiZrNbTaMo high-entropy alloy designed for orthopedic implants: As-cast microstructure and mechanical properties, Mater. Sci. Eng. C **73** (2017) 80–89.
[61] T. Nagase, M. Todai, T. Hori and T. Nakano: Microstructure of equiatomic and non-equiatomic Ti-Nb-Ta-Zr-Mo high-entropy alloys for metallic biomaterials, J. Alloy. Compd. **753** (2018) 412–421.
[62] T. Hori, T. Nagase, M. Todai, A. Matsugaki and T. Nakano: Development of non-equiatomic Ti-Nb-Ta-Zr-Mo high-entropy alloys for metallic biomaterials, Scr. Mater. **172** (2019) 83–87.
[63] T. Nagase, Y. Iijima, A. Matsugaki, K. Ameyama and T. Nakano: Design and fabrication of Ti–Zr-Hf-Cr-Mo and Ti–Zr-Hf-Co-Cr-Mo high-entropy alloys as metallic biomaterials, Mater. Sci. Eng. C **107** (2020) 110322.
[64] T. Matsuzaka, A. Hyakubu, Y.S. Kim, A. Matsugaki, T. Nagase, T.

Ishimoto, R. Ozasa, H.S. Kim, T. Mizuguchi, O. Gokcekaya and T. Nakano: Development of an equiatomic octonary TiNbTaZrMoHfWCr super-high-entropy alloy for biomedical applications, Mater. Chem. Phys. **316** (2024) 129120.

[65] Y. Lu, Y. Dong, S. Guo, L. Jiang, H. Kang, T. Wang, B. Wen, Z. Wang, J. Jie, Z. Cao, H. Ruan and T. Li: A Promising New Class of High-Temperature Alloys: Eutectic High-Entropy Alloys, Sci. Rep. **4** (2014) 6200.

[66] Y. Lu, X. Gao, L. Jiang, Z. Chen, T. Wang, J. Jie, H. Kang, Y. Zhang, S. Guo, H. Ruan, Y. Zhao, Z. Cao and T. Li: Directly cast bulk eutectic and near-eutectic high entropy alloys with balanced strength and ductility in a wide temperature range, Acta Mater. **124** (2017) 143–150.

[67] T. Nagase, M. Takemura, M. Matsumuro and T. Maruyama: Solidification Microstructure of $AlCoCrFeNi_{2.1}$ Eutectic High Entropy Alloy Ingots, Mater. Trans. **59** (2018) 255–264.